Article

Landscape-Based View on the Stepping Movement of Myosin VI

Published as part of The Journal of Physical Chemistry virtual special issue "Jose Onuchic Festschrift".

Tomoki P. Terada,*,[⊥] Qing-Miao Nie,[⊥] and Masaki Sasai*

Read Online

ACCESS | 📊 Metrics & More | 📰 Article Recommendations | 🆂🅸 Supporting Information

ABSTRACT: Myosin VI dimer walks toward the minus end of the actin filament with a large and variable step size of 25−36 nm. Two competing models have been put forward to explain this large step size. The Spudich model assumes that the myosin VI dimer associates at a distal tail near the cargo-binding domain, which makes two full-length single α-helix (SAH) domains serve as long legs. In contrast, the Houdusse−Sweeney model assumes that the association occurs in the middle (between residues 913 and 940) of the SAH domain and that the three-helix bundles unfold to ensure the large step size. Their consistency with the observation of stepping motion with a large and variable step size has not been examined in detail. To compare the two proposed models of myosin VI, we computationally characterized the free energy landscape experienced by the leading head during the stepping movement along the actin filament using the elastic network model of two heads and an implicit model of the SAH domains. Our results showed that the Spudich model is more consistent with the 25−36 nm step size than the Houdusse−Sweeney model. The unfolding of the three-helix bundles gives rise to the free energy bias toward a shorter distance between two heads. Besides, the stiffness of the SAH domain is a key factor for giving strong energetic bias toward the longer distance of stepping. Free energy analysis of the stepping motion complements the visual inspection of static structures and enables a deeper understanding of underlying mechanisms of molecular motors.
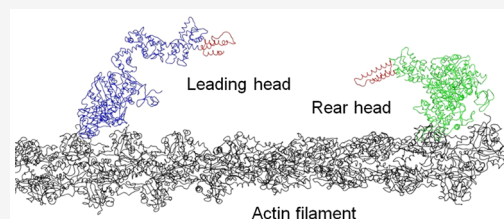
INTRODUCTION

Myosin VI is a member of the myosin superfamily, which is involved in various cellular processes.[1,2] In its monomeric form, it binds to both a cell membrane and actin filament, and in its dimeric form, it transports vesicles by processively moving toward the minus end of the actin filament through a hand-over-hand mechanism.[3−5] Here, in its dimer movement, the step size from the rear head to the leading head has been reported to be 25−36 nm.[4−10] In particular, by the high-resolution imaging, Nishikawa et al.[10] revealed the switching behavior in the dimer movement between 36 nm hand-over-hand steps and 8 nm inchworm-like steps. The step size as large as 36 nm is comparable to that of myosin V, another member of the myosin superfamily with six calmodulins within the neck domain.[11] This fact has been rather difficult to interpret because myosin VI has a much shorter neck domain than myosin V. Two models have been put forward to explain the 36 nm step size, which we here call the Spudich model[12] and the Houdusse−Sweeney model.[9] As shown in Figure 1A, the Spudich model assumes that two monomers dimerize at the cargo binding domain and that the long single α-helix (SAH) domain allows for the long stride with three-helix bundles of the proximal tail folded. In contrast, as shown in Figure 1B, the Houdusse−Sweeney model assumes that two monomers dimerize at the coiled-coil structure formed by the SAH domain and that the unfolding of the three-helix bundles

allows for the long stride. These two models are built on the structural requirement that the leading and rear heads are located 36 nm apart along the actin filament.

Because the helical pitch of the actin filament is approximately 36 nm, the frequent appearance of the 36 nm steps in observations[10] suggests that the interactions between the myosin head and the actin filament are a key determinant of the step size. Therefore, to resolve the problem of the large step size, not only the structure of myosin but also the interactions between the myosin head and the actin filament should be quantitatively assessed. Here, we should emphasize the role of entropy; not only the interaction energy but also the entropy of structural fluctuations are important for analyzing the myosin-actin interactions so that the analyses of the free energy landscape are necessary.

A stepping motion of the processive motor can be regarded as the diffusion of the leading head over the actin filament surface. Here, the leading head is tethered to the rear head, while the rear head is bound to the actin filament. Using the
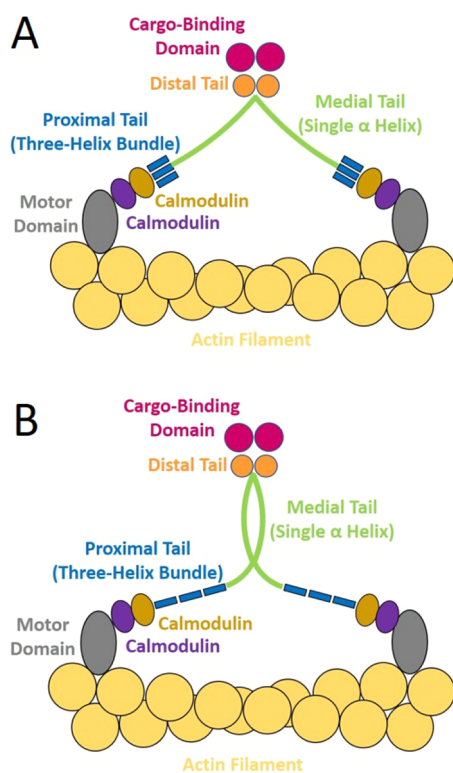
Figure 1. Schematic comparison of two models. (A) Spudich model and (B) Houdusse−Sweeney model.

experimentally determined structure of each head under the restraint arising from the tethering, we can computationally derive the free energy landscape or the potential of mean force, which guides the diffusive motion of the leading head. To consistently explain the observed 36 nm stepping motion of myosin VI, the free energy landscape is required to be biased along the actin filament toward the most stable position of the leading head located 36 nm ahead of the rear head. However, such a condition on the dynamical movement of the leading head has not been tested to compare the two proposed models. Therefore, in this paper, using the free energy landscape method, which is similar to what we have used for myosin II,[13−15] we computationally investigated whether this condition is met or not with each of the two proposed models, i.e.,

the Spudich model and the Houdusse−Sweeney model. Our results showed that the Spudich model is more consistent with the observed 25−36 nm step size than the Houdusse−Sweeney model. We also found that the folding of the three-helix bundles and the large persistence length of the SAH domain are necessary for realizing the large step size.

■ METHODS

Actin-Myosin System. We consider a system composed of two myosin heads and an actin filament. As shown in Figure 2A, the actin filament in the model is composed of 26 subunits and restrained to the model space by spring potentials. We represented the C_α atom of each amino acid residue by a bead in the myosin heads and the actin filament. Structural models of the myosin heads and the actin filament were constructed from the experimentally determined structures as explained in the Structural Models subsection of the Methods section, and the interactions between residues were represented by the elastic network, which stabilizes the structural models[13,16] as explained in the Interactions subsection of the Methods section. We examined the leading head in either the prestroke state or the poststroke state, whereas the rear head was assumed to be in the poststroke state. The motor domain of the rear head bound to the surface of the actin filament was restrained by the spring potential to a position near the plus end of the actin filament, while the leading head was assumed to interact with the actin filament by the electrostatic and van der Waals interactions.

The C-terminal residues of the rear and leading heads were connected to the two SAH domains. The recent nuclear magnetic resonance (NMR) measurements[17,18] showed that these SAH domains are stiff with a large value of the persistence length $P = 22.4$ nm. This large value of P has been attributed to the electrostatic interactions among charged side-chains in the SAH.[19] As shown later in the Results and Discussion section, the large value of P plays a crucial role in determining the bias of the movement of the leading head along the actin filament surface. In order to represent these stiff SAH domains and to examine the effect of varying the stiffness in simulations, we represented the two SAH domains by a pair of elastic rods, which can bend and twist, instead of using the conventional elastic-network representation. We assumed that these rods are connected to form a Λ-shaped structure, and
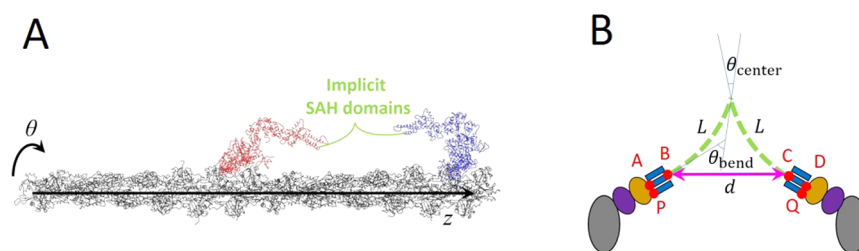

Figure 2. Simulation setup. (A) Typical snapshot showing the setup for the Langevin molecular dynamics simulations. The structures of the leading head (red) and the rear head (blue) of myosin VI and the actin filament (black) were explicitly represented by the elastic network model, whereas the SAH domains were implicitly considered as Λ-shaped elastic rods connecting the C-terminals of the two heads of myosin VI. The cylindrical coordinate system (z, θ, r) was defined around the actin filament. The rear head was bound to the filament at (z, θ) = (0 nm, 0°), and the leading head was cast toward the $z < 0$ direction. (B) Implicit representation of the two SAH domains as the Λ-shaped elastic rods. In order to represent the elastic bending and twisting of the rods in the model, we defined potential functions among six amino acid residues, A, B, C, D, P, and Q; the elastic energy of rod bending was calculated by representing the bending angle θ_{bend} as a function of the distance $d = \overline{BC}$. The center angle was fixed at its stable value as $\theta_{center} = \theta^0_{center}$ when $d \leq d^0$ with $d^0 = (4L/\pi - \theta^0_{center})\cos(\theta^0_{center}/2)$, and varied as $\theta^0_{center} < \theta_{center} \leq \pi$ when $d^0 < d \leq 2L$. See the Interactions subsection of the Methods section and the Supporting Information for details.

this configuration was represented implicitly in the model by the interactions among six amino acid residues (three amino acid residues in each head), as shown in Figure 2B. With this implicit modeling of the SAH domains, the difference between the Spudich model[12] and the Houdusse−Sweeney model[9] was expressed in terms of two parameters of the Λ-shaped elastic rods: the center angle in the stable configuration, θ_{center}^0, and the stable length of the SAH domain, L. Though the charged residues are the origin of the large stiffness of the rod, they should not give the high rigidity against twisting the rods and varying the angle between the three-helix bundle and the SAH rod. Therefore, we assumed moderate values of elastic constants for these degrees of freedom to allow flexible deformation. See the Interactions subsection of the Methods section and the Supporting Information for more details. Thus, defined implicit Λ-shaped elastic rods tether the leading head to the rear head in the model.

We performed the Langevin molecular dynamics calculation to simulate the Brownian motion of the whole system.[20] To obtain the free energy landscapes, we defined the cylindrical coordinate system around the actin filament (z, θ, r) for the mass center of the motor domain of the leading head. Here, the z-axis is parallel to the center axis of the actin filament (the filament axis) with $z > 0$ at the plus end and $z < 0$ at the minus end, θ is the angle around the filament axis, and r is the radial distance from the filament axis. We divided the three-dimensional space spanned by (z, θ, r) around the actin filament into $8 \times 7 \times 3$ blocks, and for each block, we applied an umbrella potential to enhance the sampling of that block. The thus calculated data were reweighted and combined by the weighted histogram analysis method[21] to obtain the positional distribution $P(z, \theta, r)$ of the leading head around the actin filament. From this positional distribution, we obtained the free energy landscape $F(z, \theta)$ for the leading head's position (z, θ) as $F(z, \theta) = -k_B T \log\left(\int_0^\infty dr P(z, \theta, r)\right)$, where k_B is the Boltzmann constant and $T = 300$ K is temperature. See the Supporting Information for details.

Structural Models. We constructed structural models for the myosin VI leading head, the rear head, and the actin filament. Three structural models of the myosin VI head were constructed: the prestroke structure of the leading head M_l^{pre}, the poststroke structure of the leading head M_l^{post}, and rigor-like structure of the rear head M_r^{rigor}. Each of two heads is comprised of a heavy chain and two calmodulins. M_l^{pre} is the prestroke structure of myosin VI with the bound Mg^{2+} and ADP. Because the X-ray structure of the myosin VI head including the neck domain is not yet available, we constructed M_l^{pre} by merging the motor domain of myosin VI with ADP and Mg^{2+} (PDB code: 4PFO), the converter domain of myosin VI in the prestroke state (PDB code: 4ANJ), and the myosin VI neck domain (PDB code: 3GN4) using the software MODELLER.[22] M_l^{post} is the poststroke structure of myosin VI without nucleotide or Mg^{2+}, which was constructed using the myosin VI ligand-free crystal structure (PDB code: 2BKH). Its converter domain and neck domain were modeled using myosin VI in the prestroke state (PDB code: 4ANJ) and the myosin VI neck domain structure (PDB code: 3GN4), respectively. M_r^{rigor} is the rigor-like structure of myosin VI strongly bound to actin. M_r^{rigor} was constructed using the myosin VI nucleotide-free crystal structure (PDB code:

2BKH) with its neck domain being modeled using the myosin VI neck domain structure (PDB code: 3GN4). To mimic the docking of the rear head onto the actin filament, we used the electron-microscopy structure of the myosin II-actin complex in the rigor state as a reference structure.[23] The actin filament was modeled based on the X-ray structure (PDB code: 2ZWH), and a complex of 26 subunits was prepared. All missing residues in the myosin heads and the actin were complemented by using MODELLER. In our simulation, the rear head was docked onto the positive end of the actin filament. We used the structural models M_l^{pre}, M_l^{post}, and M_r^{rigor} and the model of actin filament as reference structures for the elastic network model (see the Interactions subsection). Coordinates of structures M_l^{pre}, M_l^{post}, and M_r^{rigor} are provided in the Supporting Information 002.pdb, 003.pdb, and 004.pdb, respectively.

Interactions. The simulated system was composed of the leading head and the rear head of myosin VI and a single actin filament having 26 subunits. Each amino acid was represented as a coarse-grained particle (CP). Bound Mg^{2+} and ADP in the prestroke structure M_l^{pre} were represented by all non-hydrogen atoms, whereas M_l^{post} and M_r^{rigor} contained no ligand atoms. The total potential energy is given by

$$E_{total}(\mathbf{R}_l, \mathbf{R}_r, \mathbf{R}_a) = E_l^{intra}(\mathbf{R}_l) + E_r^{intra}(\mathbf{R}_r) + E_a^{intra}(\mathbf{R}_a)$$
$$+ E_{l-r}^{inter}(\mathbf{R}_l, \mathbf{R}_r) + E_{l-a}^{inter}(\mathbf{R}_l, \mathbf{R}_a)$$
$$+ E_a^{res}(\mathbf{R}_a) + E_r^{res}(\mathbf{R}_r) + E_l^{umb}(\mathbf{R}_l)$$

where l, r, and a denote the leading head, the rear head of myosin, and the actin filament, respectively, and E^{intra}, E^{inter}, E^{res}, and E^{umb} represent the potential energy functions for the intramolecular and intermolecular interactions, the spatial restraints, and the umbrella potentials, respectively. $\mathbf{R}_l$, $\mathbf{R}_r$, and $\mathbf{R}_a$ are Cartesian coordinates of CPs in the leading head, the rear head, and the actin filament, respectively.

The potential energy function for the intramolecular interaction was given by

$$E_x^{intra}(\mathbf{R}_x) = E_x^{ENM}(\mathbf{R}_x) + E_l^{ligand}(\mathbf{R}_l)$$

Here, $E_x^{ENM}(\mathbf{R}_x)$ is the elastic network model of proteins.[13,16] x stands for l, r, or a. In cases where the three-helix bundles are unfolded, we switched off the potentials for contacts between helices in the three-helix bundles and also for the contacts between the three-helix bundles and the other parts of the two heads of myosin VI. $E_l^{ligand}(\mathbf{R}_l)$ is the ligand contact potential for ligands Mg^{2+} and ADP within the leading head. As a whole, $E_x^{intra}(\mathbf{R}_x)$ was defined so that the reference structure is the energy-minimum structure of $E_x^{intra}(\mathbf{R}_x)$.

The leading head and the rear head were connected by two SAH domains, which were implicitly represented as Λ-shaped elastic rods. This assumption enabled us to directly examine cases with the modulated persistence length of the SAH domain. Intermolecular interactions between the leading head and the rear head were approximated by the sum of interactions as

$$E_{l-r}^{inter}(\mathbf{R}_l, \mathbf{R}_r) = E_{distance} + E_{angle} + E_{collision} + E_{torsion}$$

We labeled the position of four residues, 892 of the leading head, 909 of the leading head, 909 of the rear head, and 892 of the rear head, as A, B, C, and D, respectively. Then we
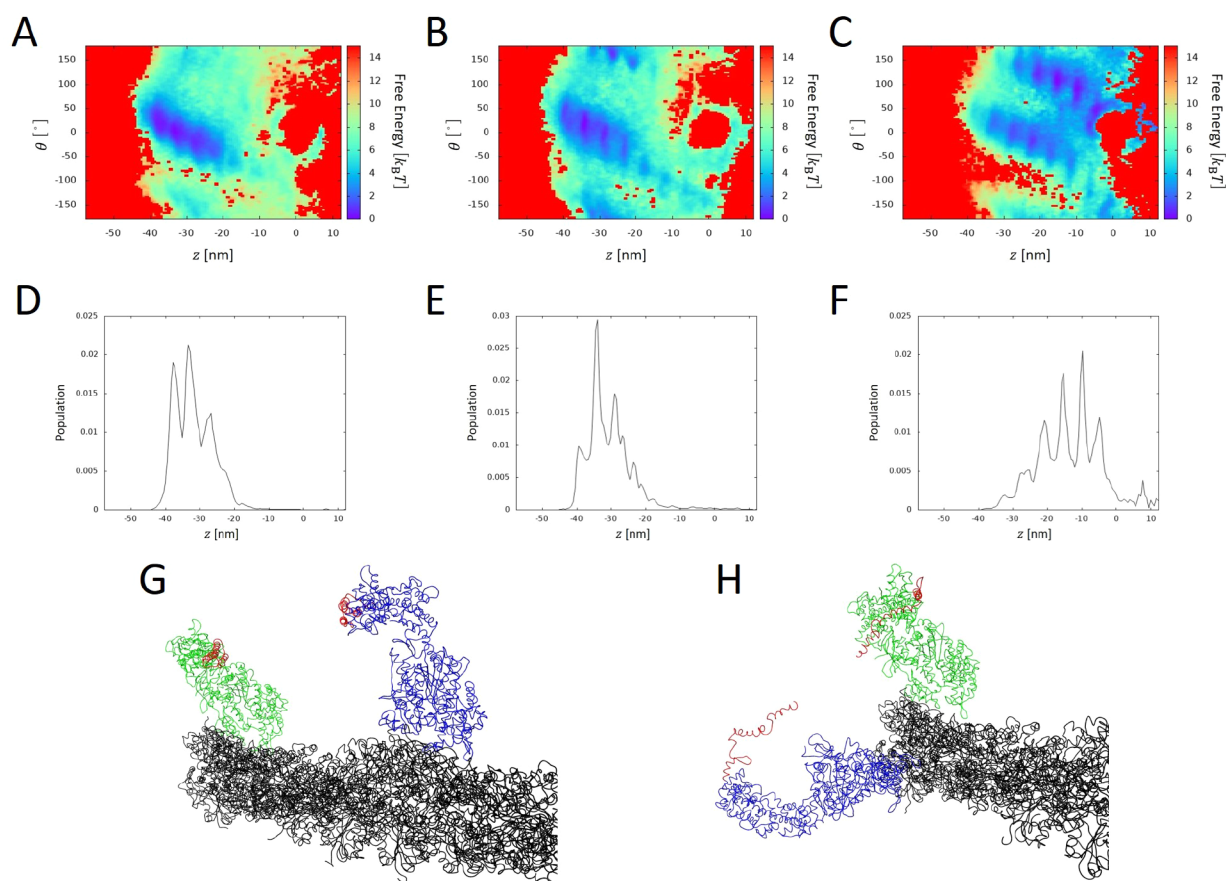
Figure 3. Free energy landscapes $F(z, \theta)$ and the step-size distributions $P(z)$. (A, B) Free energy landscapes obtained with the parameter set corresponding to the Spudich model.[12] (C) Free energy landscape obtained with the parameter set corresponding to the Houdusse−Sweeney model.[9] Leading head is in the prestroke state in A and C and in the poststroke state in B. (D) Step-size distribution derived from A, (E) the step-size distribution derived from B, and (F) the step-size distribution derived from C. (G) Snapshot structure in the Spudich model with the leading head residing at $(z, \theta) = (-33 \text{ nm}, -11°)$ near the minimum in the free energy landscape A, and (H) a snapshot structure in the Houdusse−Sweeney model with the leading head residing at $(z, \theta) = (-6 \text{ nm}, 108°)$ near the minimum in the free energy landscape C. In G and H, the three-helix bundles in the leading and rear heads are colored red, the other part of the leading head is blue, and the other part of the rear head is green; the actin filament is black and the implicit SAH domains connecting the leading and rear heads are not drawn.

considered the interactions between the two vectors $\overrightarrow{BA}$ and $\overrightarrow{CD}$. The energy which is dependent only on the distance $d = \overline{BC}$ was given by

$$E_{\text{distance}} = E_{\text{bend}}\Theta(2L - d)$$
$$+ E_{\text{open}}\Theta(2L - d)\Theta\left(d - \frac{4L}{\pi - \theta^0_{\text{center}}} \cos \frac{\theta^0_{\text{center}}}{2}\right)$$

where we used Heaviside's function $\Theta(x) = 1$ for $x \geq 0$ and $\Theta(x) = 0$ for $x < 0$. For $d \leq 2L$, the bending energy of the two elastic rods with the bending angle θ_{bend} is given by $E_{\text{bend}} = 2\frac{Pk_{\text{B}}T\theta_{\text{bend}}(d)^2}{2L}$, where P is the persistence length of the SAH domains, L is the length of each elastic rod, and the prefactor of 2 comes from the number of elastic rods in the system. For $0 \leq d \leq \frac{4L}{\pi - \theta^0_{\text{center}}} \cos \frac{\theta^0_{\text{center}}}{2}$, we assumed that the center angle θ_{center} of the Λ-shaped elastic rods is equal to a constant θ^0_{center}. For $\frac{4L}{\pi - \theta^0_{\text{center}}} \cos \frac{\theta^0_{\text{center}}}{2} < d \leq 2L$, we assumed that the center angle θ_{center} becomes larger than θ^0_{center} while the other ends (at points B and C) are kept parallel with the straight line BC. This extra opening angle was accompanied by

the penalty energy function as $E_{\text{open}} = k_{\text{open}}(\theta_{\text{center}} - \theta^0_{\text{center}})^2$ for $\theta_{\text{center}} > \theta^0_{\text{center}}$. For $d > 2L$, $\theta_{\text{center}} = \pi$ and we considered that two points B and C are pulled toward each other by a spring potential, $E_{\text{pull}} = k_{\text{pull}}(d - 2L)^2$.

The angles θ_{ABC} and θ_{BCD} were subject to the angle potential as $E_{\text{angle}} = k_{\text{angle}}(\theta_{\text{ABC}} - \theta^0_{\text{angle}}(d))^2 + k_{\text{angle}}(\theta_{\text{BCD}} - \theta^0_{\text{angle}}(d))^2$. We also considered the collision potential as $E_{\text{collision}} = K_{\text{collision}}(\delta - r_{\text{th}})^2 \; (\delta < r_{\text{th}})$, or $0 \; (\delta \geq r_{\text{th}})$, where δ is the nearest distance of the line segment BC from the z-axis, and r_{th} is a threshold distance. We further defined the torsional potential energy as $E_{\text{tortion}} = \frac{1}{2}k_{\text{tortion}}\left(\frac{\theta_{\text{twist}}}{2L}\right)^2 2L = \frac{k_{\text{tortion}}}{4L}\theta^2_{\text{twist}}$ where θ_{twist} is the twisting angle of two SAH domains (see the Supporting Information for the definition).

The potential energy $E^{\text{inter}}_{\text{l−a}}(\boldsymbol{R}_{\text{l}}, \boldsymbol{R}_{\text{a}})$ for the intermolecular interaction between the leading head and the actin filament was composed of the Debye−Hückel electrostatic interactions and the van der Waals interactions.

The restraint potentials applied to the actin filament and the motor domain of the rear head were given, respectively, by
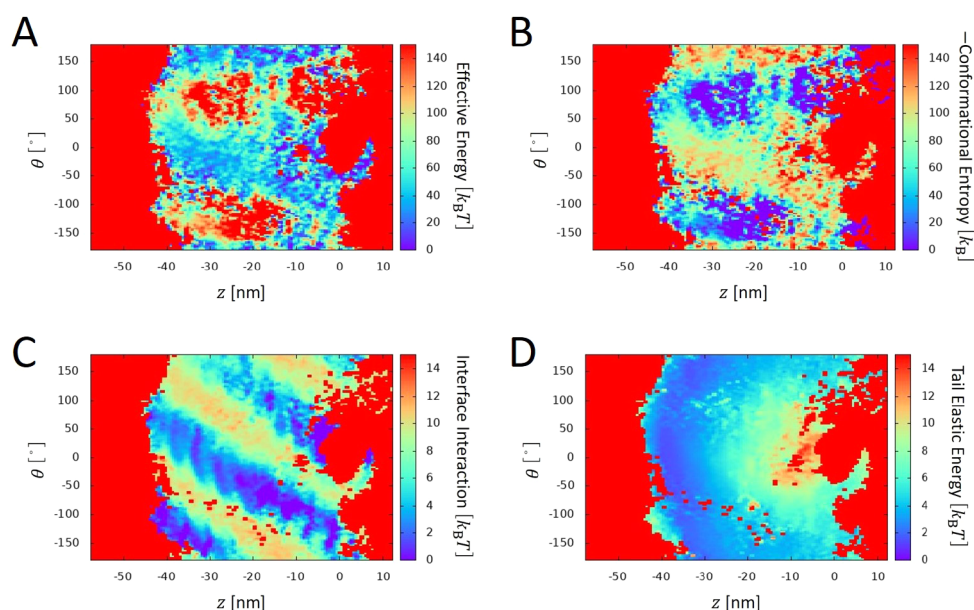
Figure 4. Decomposition of free energy obtained with the Spudich model[12] into contributions from energies and the conformational entropy. The free energy landscape $F(z, \theta) = E(z, \theta) - TS(z, \theta)$ of Figure 3A is decomposed into (A) the effective energy landscape $E(z, \theta)$ and (B) the conformational entropy landscape $-S(z, \theta)$. (C) The landscape of the myosin-actin interface energy, and (D) the landscape of the elastic energy of the SAH domains.

$$E_a^{res}(\mathbf{R}_a) = \sum \frac{k_{a,res}}{2}[(x_{a,i} - x_{a,i}^0)^2 + (y_{a,i} - y_{a,i}^0)^2 + (z_{a,i} - z_{a,i}^0)^2]$$

and

$$E_r^{res}(\mathbf{R}_r) = \sum \frac{k_{r,res}}{2}[(x_{r,i} - x_{r,i}^0)^2 + (y_{r,i} - y_{r,i}^0)^2 + (z_{r,i} - z_{r,i}^0)^2]$$

where $(x_{a,i}^0, y_{a,i}^0, z_{a,i}^0)$ and $(x_{r,i}^0, y_{r,i}^0, z_{r,i}^0)$ are the coordinates of the reference structures (see the Structural Models subsection). See the Supporting Information for more details.

RESULTS AND DISCUSSION

Free Energy Landscape of the Two Models. Figure 3A shows the free energy landscape, $F(z, \theta)$, of the position of the leading head in the prestroke state obtained with the parameter set corresponding to the Spudich model.[12] The stable center angle between two SAH domains is $\theta_{center}^0 = 160°$, the stable length of each SAH domain is $L = 94.5$ Å (corresponding to the residues 918−980), and the three-helix bundles are folded. The value of θ_{center}^0 has not been directly measured in the experiments, but the value used here is consistent with the model structure derived from the small-angle X-ray scattering (SAXS) data of the myosin VI monomer[12] and the electron microscope image of the myosin VI dimer showing the large center angle.[24]

The free energy landscape in Figure 3A has a basin at around $z \approx -20 \sim -40$ nm at $\theta \approx 0°$, showing that the Spudich model gives a strong bias toward the position 36 nm ahead in the minus-end direction from the rear head bound at $(z, \theta) \simeq (0$ nm, 0°). The large width of the basin is consistent with the experimentally observed width of the 25−36 nm step size,[4−10] and a distinct lowering of the free energy at $z \approx -36$ nm is

consistent with the observation of 36 nm steps.[10] This bias for the leading-head motion is confirmed by calculating the distribution of the position of the leading head, $P(z) \propto \int d\theta \exp(-F(z, \theta)/(k_B T))$; the large width of $P(z)$ shown in Figure 3D is consistent with the experimentally observed broad distribution of the step size.[4−10]

Figure 3B,E shows the free energy landscape and the step-size distribution in the case that the leading head is in the poststroke state in the Spudich model. Figure 3A,D and Figure 3B,E show that the Spudich model gives a strong bias toward the position 36 nm ahead from the rear head. However, in Figure 3B, another basin exists on the opposite side of the actin filament ($\theta \approx 180°$). The single molecule experiment[25] has shown that myosin VI walks almost parallel to the actin filament for more than 1 μm without rotating around the actin filament, which is more consistent with Figure 3A than with Figure 3B, suggesting that the stepping motion of myosin VI occurs when the leading head is in the prestroke state, which is consistent with the commonly accepted hand-overhand model.

Figure 3C,F shows the free energy landscape and the step-size distribution obtained with the Houdusse−Sweeney model.[9] The stable center angle between two SAH domains is $\theta_{center}^0 = 20°$, which corresponds to the value within the helix bundle, and the stable length of each SAH domain is $L = 34.5$ Å (corresponding to the residues 918−940). In the Houdusse−Sweeney model, we assumed that interactions between helices in each three-helix bundle are turned off with thermal fluctuations. With this disappearance of interactions in the model, the three-helix bundles are unfolded, leading to the extension of the end-to-end distance of this region.[26] As shown later in the Results and Discussion section, using the large values of $\theta_{center}^0 = 160°$ and $L = 94.5$ Å does not significantly alter the free energy landscape as far as the three-helix bundles are unfolded (Figure 6); hence, the unfolding of the three-helix bundles characterizes the main features of the free energy landscape in the Houdusse−Sweeney model.
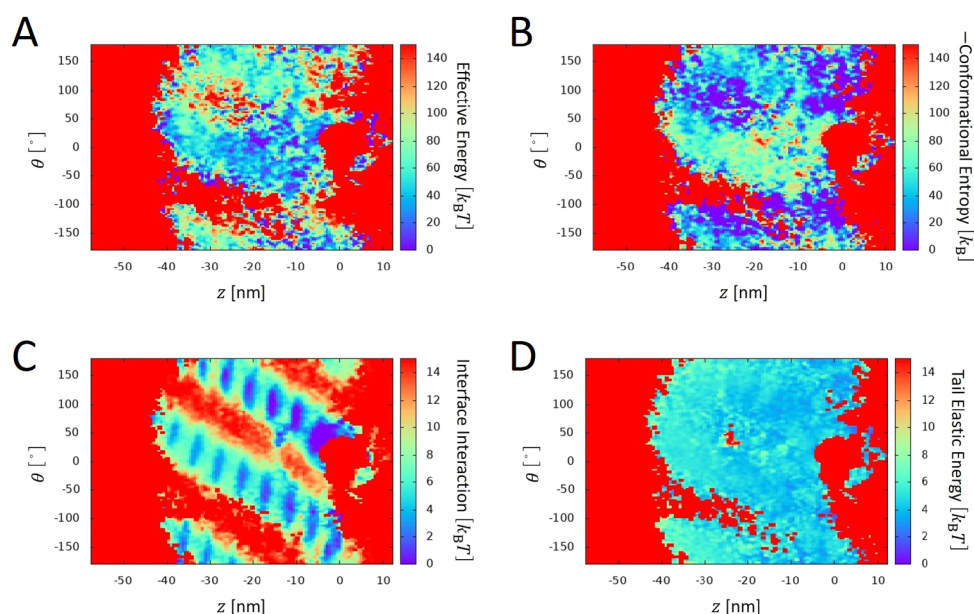
Figure 5. Decomposition of free energy obtained with the Houdusse−Sweeney model[9] into contributions from energies and the conformational entropy. Free energy landscape $F(z, \theta) = E(z, \theta) − TS(z, \theta)$ of Figure 3C is decomposed into (A) the effective energy landscape, $E(z, \theta)$, and (B) the conformational entropy landscape, $−S(z, \theta)$. (C) Landscape of the myosin−actin interface energy, and (D) the landscape of the elastic energy of the SAH domains.

Figure 3C,F shows the case in which the leading head is in the prestroke state, and Figure S1 shows the case in which the leading head is in the poststroke state. The lowest free energy minimum is located at $(z, \theta) \simeq (− 16 \text{ nm}, 120°)$ and $(z, \theta) \simeq (− 21 \text{ nm}, 130°)$ in Figure 3C and Figure S1, respectively. As compared to Figure 3A, there is no free energy bias toward 36 nm ahead from the rear head, and the free energy minimum shifted much closer to the rear head and on the opposite side of the actin filament. These positions of the free energy minima are inconsistent with the 36 nm step size[10] or the 27 nm step size reported by the Houdusse−Sweeney group.[8,9] Besides, the free energy basin on the opposite side of the actin filament is more pronounced than in Figure 3B, which contradicts the experimental finding that myosin VI walks almost parallel to the actin filament without rotating around the actin filament.[25] Figure 3G,H compares the snapshot structures with the leading head residing near the free energy minimum in the Spudich and the Houdusse−Sweeney models. We found that the Houdusse−Sweeney model allows flexible helix deformation, enabling the wide structural exploration of the leading head reaching the loci on the opposite side of the actin filament (Figure 3H). In contrast, the Spudich model's folded three-helix bundles suppress such a broad structural exploration unless a significant SAH deformation is induced (Figure 3G). Figure S2 shows the free energy landscape when the value of the elastic constant of the twisting deformation of the SAH domains, k_{tortion}, is doubled from the standard value in the Houdusse−Sweeney model. Figure S2 shows no significant difference from Figure 3C, indicating that the rigid SAH domains do not prevent the wide structural exploration of the leading head when three-helix bundles are unfolded. Comparing Figure 3A and Figure 3C, the Spudich model is more consistent with the observed 36 nm step than the Houdusse−Sweeney model.

Dissecting the Differences between the Two Models. We can analyze the balance between energy and entropy by decomposing the free energy landscapes in Figure 3. By

decomposing the free energy landscape $F(z, \theta) = E(z, \theta) − TS(z, \theta)$ of Figure 3A calculated with the Spudich model, we obtained the landscape of effective energy $E(z, \theta)$ (Figure 4A) and the landscape of conformational entropy $−S(z, \theta)$ (Figure 4B). Here, $E(z, \theta)$ was calculated by $E(z, \theta) = \int dr E_{\text{total}}(z, \theta, r) P(z, \theta, r)$ with $E_{\text{total}}(z, \theta, r)$ being $E_{\text{total}}(\boldsymbol{R}_l, \boldsymbol{R}_r, \boldsymbol{R}_a)$ averaged over $\boldsymbol{R}_l$, $\boldsymbol{R}_r$, and $\boldsymbol{R}_a$ under the constraint of the leading-head's position (z, θ, r), and $S(z, \theta)$ was calculated as $S(z, \theta) = \frac{1}{T}(E(z, \theta) − F(z, \theta))$. We should note that with the present coarse-grained representation, entropy of the solvent water molecules and side-chain atomic fluctuations are renormalized into the effective energy, $E(z, \theta)$, and $S(z, \theta)$ represents the rest effects, i.e., the effects of fluctuations of the main-chain conformation. Comparing these figures, we find that the energetic and entropic contributions are largely compensated with each other; it is intriguing to find that the effective energy is low at $z \approx 0$ at the position for the inchworm-like stepping, but the conformational entropy of this position is small to prohibit the inchworm-like stepping in the present calculation. Entropy is large at $\theta \approx \pm 120°$, but this entropically favored position is high in energy and is not realized in the present case. The subtle balance between energy and entropy at $\theta \approx 0°$ gives rise to the shape of the free energy landscape, and the bias toward the position 36 nm ahead of the rear head. We can see that the overall basin in Figure 3A is stabilized by the low energy at the basin position with a mild amount of conformational entropy.

Abstracting contributions from the energy landscape of Figure 4A further provides insights into the mechanism in the free energy landscape; Figure 4C shows the contribution of the interface interactions between the leading head and the actin filament, and Figure 4D shows the contribution of the elastic energy of the SAH domains. The interface energy of Figure 4C has an array of bumps arranged with a distance of ∼5.5 nm, which is the actin subunit diameter. The relatively small entropy at these bumps (Figure 4B) smears the bumps in the

free energy landscape of Figure 3A at $\theta \approx 0°$, reducing their height to about $1k_BT$, which can be easily surmounted with thermal fluctuation. This fine feature in the free energy landscape might disappear with the effects of the structural fluctuations that are not considered in the elastic network model, leading to a smooth distribution of the leading-head movement observed in the experiments.[4−10] The interface energy landscape of Figure 4C has a basin at $z = −20 \sim −10$ nm, which provides the bias of the movement of the leading head toward the $z < 0$ direction. Figure 4D shows that the elastic energy of the SAH domains further pushes the leading head toward the $z < 0$ direction, realizing the large step size of 36 nm. In the present dimeric myosin system, the leading head is tethered to the rear head, which casts the leading head toward the minus end of the actin filament. This structural restraint brings about the bias of the energy landscape in Figure 4C,D and allows the mildly large entropy at $z \approx −30 \sim −40$ nm at $\theta \approx 0°$ (Figure 4B). Therefore, this structural restraint determines how energy and entropy are compensated, which gives rise to the global bias of the free energy toward the minus end.

The absence of such structural restraint makes a single-head movement of myosin II different from the dimer movement of myosin VI. In a single-head movement of myosin II, the motor head is not cast to either end of the actin filament. We have previously calculated the free energy landscape of a single-head myosin II with the essentially same methods as the present study and obtained the globally biased free energy landscape toward the plus end of the actin filament.[14,15] This bias in the myosin II landscape resulted from the electrostatic interactions at myosin and the actin filament interface. This free energy bias is consistent with the biased Brownian motion toward the plus end of the actin filament, which was observed in the single-molecule experiments[27−29] as well as molecular dynamics simulations.[13] Furthermore, for myosin II, the free energy landscape calculation showed an array of bumps with a ∼5.5 nm distance and ∼$3k_BT$ height,[14,15] consistent with the observed[27,28] and simulated[13] substeps of the myosin II motion. The relatively large bumps in the free energy landscape of myosin II should be due also to the energy-entropy compensation different from that in myosin VI.

Thus, the structural restraint of dimeric myosin VI determines how energy and entropy are compensated, which gives rise to the global bias of the free energy toward the minus end and the large step size in the Spudich model. We also decomposed the free energy landscape obtained with the Houdusse−Sweeney model in Figure 3C into the effective energy and the conformational entropy in Figure 5A,B, respectively. Differences between the two models are clarified in the analysis of the contributions from the interface energy (Figure 5C) and the elastic energy of the SAH domains (Figure 5D) with the Houdusse−Sweeney model. The interface energy landscape or the elastic energy landscape does not have a bias toward the $z < 0$ direction but shows the lowest energy at $z \approx 0$.

To further investigate what controls the shape of the free energy landscape, we divide the difference between the Spudich model and the Houdusse−Sweeney model into two factors: the topology of the Λ-shaped SAH domains and the folding/unfolding of the three-helix bundles. To elucidate the effect of these two factors on the free energy landscape, we conducted the calculation for the Spudich model except that the three-helix bundles are unfolded and the Houdusse−

Sweeney model except that the three-helix bundles are folded. Figure 6A shows the free energy landscape for the Spudich
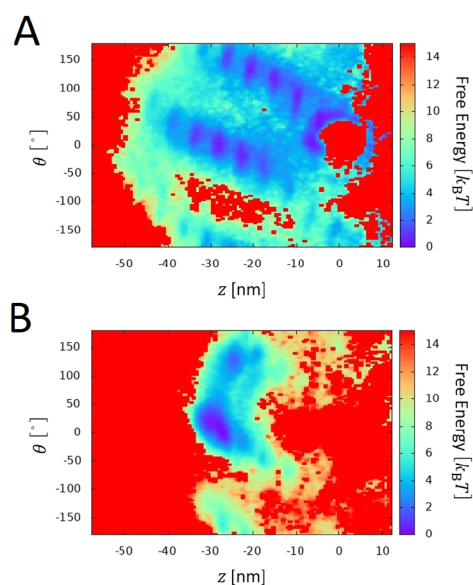

Figure 6. Free energy landscapes with the altered folding/unfolding states of the three-helix bundles. (A) Free energy landscape obtained for the Spudich model except that the three-helix bundles are unfolded, and (B) free energy landscape obtained for the Houdusse−Sweeney model except that the three-helix bundles are folded. The leading head is in the prestroke state.

model except that the three-helix bundles are unfolded. Figure 6A shows the case in which the leading head is in the prestroke state, and Figure S3 shows the case in which the leading head is in the poststroke state. In both cases, the free energy basin is much broader and the step size gets much shorter than the original Spudich model. Besides, the free energy basin on the opposite side of the actin filament is pronounced. These results suggest that the unfolding of the three-helix bundles adds more flexibility to the connection between the two heads, making the leading head move both sides of the actin filament with similar probabilities over the step size much shorter than 25−36 nm. The similarity of Figure 6A to Figure 3C suggests that the folding/unfolding of the three-helix bundles largely explains the difference in the free energy landscape between the Spudich and the Houdusse−Sweeney models.

Figure 6B shows the free energy landscape obtained for the Houdusse−Sweeney model, except that the three-helix bundles are folded. Figure 6B shows the case in which the leading head is in the prestroke state, and Figure S4 shows the case in which the leading head is in the poststroke state. In both cases, there is a narrow basin at $(z, \theta) \simeq (− 28$ nm$, 20°)$, which is consistent with the 27 nm steps[8,9] but not with the 36 nm steps.[10] The free energy basin gets much narrower compared to the other cases above, and this result is inconsistent with the experimentally observed variable step size of 25−36 nm.[4−10]

Effect of the Persistence Length of the SAH Domain. The SAH domain of myosin VI is one of the ER/K α-helix motifs, which are stabilized by dynamic interactions among charged residues.[19] From a recent NMR spectroscopy, it has been reported to be rigid with a persistence length of 22.4 nm,[17,18] which is close to the corresponding value of 15 nm of Kelch ER/K α-helix, another member of the ER/K α-helix motif.[30] However, the dynamic interactions among charged

residues, and hence the rigidity of the SAH domain, may vary depending on the experimental condition, such as the ionic strength. To investigate the effect of the persistence length variation of the SAH domain on the stepping motion of the leading head, we calculated the same free energy landscapes for the Spudich model with the persistence length modified from 22.4 to 5 nm. Figure 7 shows the case in which the leading
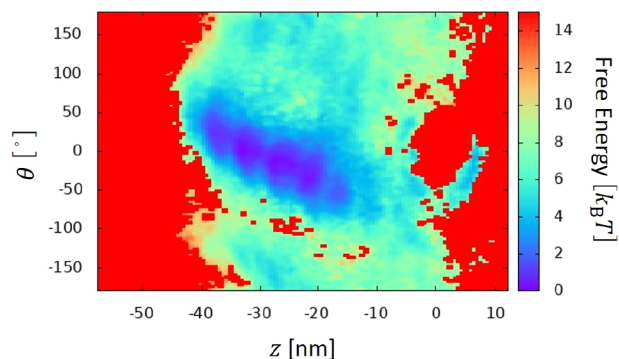

Figure 7. Free energy landscape for the Spudich model with the persistence length modified from 22.4 to 5 nm. The leading head is in the prestroke state.

head is in the prestroke state, and Figure S5 shows the case in which the leading head is in the poststroke state. As shown in Figures 7 and S4, the free energy basin remained broad, corresponding to the variable step size, but the position of the lowest free energy minimum was moved to $(z, \theta) \simeq (-28$ nm, $-20°)$, consistent with the 27 nm step size[8,9] but not with the 36 nm step size.[10] This result suggests the significant role of the persistence length in determining the step size, and the difference in the experimentally measured step sizes may have resulted from the change in the persistence length of the SAH domain depending on the experimental conditions, e.g., ionic strength.

CONCLUSION

In this work, we compared the two existing models of myosin VI, i.e., the Spudich model and the Houdusse−Sweeney model, from the free energy landscape perspective. We calculated the free energy landscapes of the leading head of myosin VI with the coarse-grained model of two heads and the simplified model of the two SAH domains connecting the two heads. A strong bias toward the 36 nm step from the rear head was observed only with the Spudich model, not the Houdusse−Sweeney model. Folding the three-helix bundles seems necessary for the strong bias toward the 36 nm step. The persistence length of the SAH domain affects the step size.

The picture of the free energy landscape developed in this paper should be applied to various other molecular motors, which move in the presence of intermolecular interaction and restraints. For myosin II, the biased Brownian motion with substeps observed in the single-molecule experiment[27,28] has been explained by the biased free energy landscape with multiple bumps.[14,15] For kinesin, the complex time evolution of the averaged displacement[31] has been linked to the broad distribution of the sideway intermediates of stepping inferred from the free energy landscape calculation.[32] Likewise, the free energy landscape calculation should be informative for understanding the foot stomp events observed in high-speed atomic force microscopy of myosin V.[33] Contributions of the

lever-arm swing and the biased Brownian motion to the myosin II movement[29] should be dissected by the free energy landscape analyses. The importance of the free energy analyses of these systems suggests that the overall reaction cycle of molecular machines should be investigated by analyzing the dynamical free energy landscape,[15,32,34−38] which considers both dynamic transitions among multiple states of chemical reaction kinetics and stochastic conformational dynamics in individual states.

The results in the present paper showed that the free energy analyses of the motion of interacting proteins complement the visual inspection of static structures and enable a deeper understanding of the underlying mechanisms of molecular motors.

■ ASSOCIATED CONTENT

Ⓢ Supporting Information

The Supporting Information is available free of charge at https://pubs.acs.org/doi/10.1021/acs.jpcb.2c03694.

> Computational details, a table summarizing the parameters in the model, the free energy landscapes for the Spudich model and the Houdusse−Sweeney model with the leading head in the poststroke state, and the free energy landscape for the Houdusse−Sweeney model with the larger elastic constant for the twisting deformation of SAH with the leading head in the prestroke state (PDF)
>
> Coordinates of the structure M_l^{pre} (PDB)
>
> Coordinates of the structure M_l^{post} (PDB)
>
> Coordinates of the structure M_r^{rigor} (PDB)

■ AUTHOR INFORMATION

Corresponding Authors

Tomoki P. Terada − *Department of Applied Physics, Nagoya University, Nagoya 464-8603, Japan;* ◎ orcid.org/0000-0001-8231-9274; Phone: +81(0)52 789 3721; Email: terada@nagoya-u.jp; Fax: +81(0)52 789 3719

Masaki Sasai − *Department of Applied Physics, Nagoya University, Nagoya 464-8603, Japan; Department of Complex Systems Science, Nagoya University, Nagoya 464-8601, Japan; Fukui Institute for Fundamental Chemistry, Kyoto University, Kyoto 606-8103, Japan;* ◎ orcid.org/0000-0002-1028-8242; Email: masakisasai@nagoya-u.jp

Author

Qing-Miao Nie − *Department of Applied Physics, Zhejiang University of Technology, Hangzhou 310023, P.R. China*

Complete contact information is available at:
https://pubs.acs.org/10.1021/acs.jpcb.2c03694

Author Contributions

⊥T.P.T. and Q.-M.N. contributed equally to this work

Notes

The authors declare no competing financial interest.

■ ACKNOWLEDGMENTS

■ REFERENCES

(1) Buss, F.; Spudich, G.; Kendrick-Jones, J. Myosin VI: cellular functions and motor properties. *Annu. Rev. Cell Dev. Biol.* **2004**, *20*, 649−676.

(2) Sweeney, H. L.; Houdusse, A. What can myosin VI do in cells? *Curr. Opin. Cell Biol.* **2007**, *19*, 57−66.

(3) Wells, A. L.; Lin, A. W.; Chen, L.-Q.; Safer, D.; Cain, S. M.; Hasson, T.; Carragher, B. O.; Milligan, R. A.; Sweeney, H. L. Myosin VI is an actin-based motor that moves backwards. *Nature* **1999**, *401*, 505−508.

(4) Rock, R. S.; Rice, S. E.; Wells, A. L.; Purcell, T. J.; Spudich, J. A.; Sweeney, H. L. Myosin VI is a processive motor with a large step size. *Proc. Natl. Acad. Sci. U.S.A.* **2001**, *98*, 13655−13659.

(5) Nishikawa, S.; Homma, K.; Komori, Y.; Iwaki, M.; Wazawa, T.; Hikikoshi Iwone, A.; Saito, J.; Ikebe, R.; Katayama, E.; Yanagida, T.; Ikebe, M.; et al. Class VI myosin moves processively along actin filaments backward with large steps. *Biochem. Biophys. Res. Commun.* **2002**, *290*, 311−317.

(6) Altman, D.; Sweeney, H. L.; Spudich, J. A. The mechanism of myosin VI translocation and its load-induced anchoring. *Cell* **2004**, *116*, 737−749.

(7) Ökten, Z.; Churchman, L. S.; Rock, R. S.; Spudich, J. A. Myosin VI walks hand-over-hand along actin. *Nat. Str. Mol. Biol.* **2004**, *11*, 884−887.

(8) Park, H.; Ramamurthy, B.; Travaglia, M.; Safer, D.; Chen, L.-Q.; Franzini-Armstrong, C.; Selvin, P. R.; Sweeney, H. L. Full-length myosin VI dimerizes and moves processively along actin filaments upon monomer clustering. *Mol. Cell* **2006**, *21*, 331−336.

(9) Mukherjea, M.; Llinas, P.; Kim, H.; Travaglia, M.; Safer, D.; Ménétrey, J.; Franzini-Armstrong, C.; Selvin, P. R.; Houdusse, A.; Sweeney, H. L. Myosin VI dimerization triggers an unfolding of a three-helix bundle in order to extend its reach. *Mol. Cell* **2009**, *35*, 305−315.

(10) Nishikawa, S.; Arimoto, I.; Ikezaki, K.; Sugawa, M.; Ueno, H.; Komori, T.; Iwane, A. H.; Yanagida, T. Switch between large hand-over-hand and small inchworm-like steps in myosin VI. *Cell* **2010**, *142*, 879−888.

(11) Yildiz, A.; Forkey, J. N.; McKinney, S. A.; Ha, T.; Goldman, Y. E.; Selvin, P. R. Myosin V walks hand-over-hand: single fluorophore imaging with 1.5-nm localization. *Science* **2003**, *300*, 2061−2065.

(12) Spink, B. J.; Sivaramakrishnan, S.; Lipfert, J.; Doniach, S.; Spudich, J. A. Long single α-helical tail domains bridge the gap between structure and function of myosin VI. *Nat. Str. Mol. Biol.* **2008**, *15*, 591.

(13) Takano, M.; Terada, T. P.; Sasai, M. Unidirectional Brownian motion observed in an in silico single molecule experiment of an actomyosin motor. *Proc. Natl. Acad. Sci. U.S.A.* **2010**, *107*, 7769−7774.

(14) Nie, Q.-M.; Sasai, M.; Terada, T. P. Conformational flexibility of loops of myosin enhances the global bias in the actin−myosin interaction landscape. *Phys. Chem. Chem. Phys.* **2014**, *16*, 6441−6447.

(15) Nie, Q.-M.; Togashi, A.; Sasaki, T. N.; Takano, M.; Sasai, M.; Terada, T. P. Coupling of lever arm swing and biased Brownian motion in actomyosin. *PLoS Comp. Biol.* **2014**, *10*, No. e1003552.

(16) Atilgan, A. R.; Durell, S.; Jernigan, R. L.; Demirel, M. C.; Keskin, O.; Bahar, I. Anisotropy of fluctuation dynamics of proteins with an elastic network model. *Biophys. J.* **2001**, *80*, 505−515.

(17) Barnes, C. A.; Shen, Y.; Ying, J.; Takagi, Y.; Torchia, D. A.; Sellers, J. R.; Bax, A. Remarkable rigidity of the single α-helical domain of myosin-VI as revealed by NMR spectroscopy. *J. Am. Chem. Soc.* **2019**, *141*, 9004−9017.

(18) Barnes, C. A.; Shen, Y.; Ying, J.; Bax, A. Modulating the stiffness of the myosin VI single α-helical domain. *Biophys. J.* **2020**, *118*, 1119−1128.

(19) Sivaramakrishnan, S.; Spink, B. J.; Sim, A. Y.; Doniach, S.; Spudich, J. A. Dynamic charge interactions create surprising rigidity in the ER/K α-helical protein motif. *Proc. Natl. Acad. Sci. U.S.A.* **2008**, *105*, 13356−13361.

(20) Honeycutt, J.; Thirumalai, D. The nature of folded states of globular proteins. *Biopolymers* **1992**, *32*, 695−709.

(21) Kumar, S.; Rosenberg, J. M.; Bouzida, D.; Swendsen, R. H.; Kollman, P. A. The weighted histogram analysis method for free-energy calculations on biomolecules. I. The method. *J. Comput. Chem.* **1992**, *13*, 1011−1021.

(22) Šali, A.; Blundell, T. L. Comparative protein modelling by satisfaction of spatial restraints. *J. Mol. Biol.* **1993**, *234*, 779−815.

(23) Lorenz, M.; Holmes, K. C. The actin-myosin interface. *Proc. Natl. Acad. Sci. U.S.A.* **2010**, *107*, 12529−12534.

(24) Phichith, D.; Travaglia, M.; Yang, Z.; Liu, X.; Zong, A. B.; Safer, D.; Sweeney, H. L. Cargo binding induces dimerization of myosin VI. *Proc. Natl. Acad. Sci. U.S.A.* **2009**, *106*, 17320−17324.

(25) Ali, M. Y.; Homma, K.; Iwane, A. H.; Adachi, K.; Itoh, H.; Kinosita, K., Jr; Yanagida, T.; Ikebe, M. Unconstrained steps of myosin VI appear longest among known molecular motors. *Biophys. J.* **2004**, *86*, 3804−3810.

(26) Magistrati, E.; Polo, S. Myomics: myosin VI structural and functional plasticity. *Curr. Opin. Str. Biol.* **2021**, *67*, 33−40.

(27) Kitamura, K.; Tokunaga, M.; Iwane, A. H.; Yanagida, T. A single myosin head moves along an actin filament with regular steps of 5.3 nanometres. *Nature* **1999**, *397*, 129−134.

(28) Kitamura, K.; Tokunaga, M.; Esaki, S.; Hikikoshi Iwane, A.; Yanagida, T. Mechanism of muscle contraction based on stochastic properties of single actomyosin motors observed in vitro. *Biophys* **2005**, *1*, 1−19.

(29) Fujita, K.; Ohmachi, M.; Ikezaki, K.; Yanagida, T.; Iwaki, M. Direct visualization of human myosin II force generation using DNA origami-based thick filaments. *Comm. Biol.* **2019**, *2*, 437.

(30) Sivaramakrishnan, S.; Sung, J.; Ali, M.; Doniach, S.; Flyvbjerg, H.; Spudich, J. Combining single-molecule optical trapping and small-angle x-ray scattering measurements to compute the persistence length of a protein ER/K α-helix. *Biophys. J.* **2009**, *97*, 2993−2999.

(31) Nishiyama, M.; Muto, E.; Inoue, Y.; Yanagida, T.; Higuchi, H. Substeps within the 8-nm step of the ATPase cycle of single kinesin molecules. *Nat. Cell Biol.* **2001**, *3*, 425−428.

(32) Hyeon, C.; Onuchic, J. N. Mechanical control of the directional stepping dynamics of the kinesin motor. *Proc. Natl. Acad. Sci. U.S.A.* **2007**, *104*, 17382−17387.

(33) Kodera, N.; Yamamoto, D.; Ishikawa, R.; Ando, T. Video imaging of walking myosin V by high-speed atomic force microscopy. *Nature* **2010**, *468*, 72−76.

(34) Kumar, S.; Ma, B.; Tsai, C.-J.; Sinha, N.; Nussinov, R. Folding and binding cascades: dynamic landscapes and population shifts. *Protein Sci.* **2000**, *9*, 10−19.

(35) Koga, N.; Takada, S. Folding-based molecular simulations reveal mechanisms of the rotary motor F1−ATPase. *Proc. Natl. Acad. Sci. U.S.A.* **2006**, *103*, 5367−5372.

(36) Terada, T. P.; Kimura, T.; Sasai, M. Entropic mechanism of allosteric communication in conformational transitions of dihydrofolate reductase. *J. Phys. Chem. B* **2013**, *117*, 12864−12877.

(37) Berezhkovskii, A. M.; Makarov, D. E. From nonequilibrium single-molecule trajectories to underlying dynamics. *J. Phys. Chem. Lett.* **2020**, *11*, 1682−1688.

(38) Okazaki, K.; Nakamura, A.; Iino, R. Chemical-state-dependent free energy profile from single-molecule trajectories of biomolecular motors: Application to processive Chitinase. *J. Phys. Chem. B* **2020**, *124*, 6475−6487.